Organization and dynamics of the nonhomologous end-joining machinery during DNA double-strand break repair

Dylan A. Reid[a], Sarah Keegan[a], Alejandra Leo-Macias[a], Go Watanabe[b], Natasha T. Strande[c], Howard H. Chang[b], Betul Akgol Oksuz[a], David Fenyo[a], Michael R. Lieber[b], Dale A. Ramsden[c], and Eli Rothenberg[a,1]

[a]Department of Biochemistry and Molecular Pharmacology, New York University School of Medicine, New York, NY 10016; [b]Department of Pathology, Biochemistry & Molecular Biology, Molecular Microbiology & Immunology, USC Norris Comprehensive Cancer Center, Keck School of Medicine, University of Southern California, Los Angeles, CA 90089; and [c]Department of Biochemistry and Biophysics, Lineberger Comprehensive Cancer Center, University of North Carolina School of Medicine, Chapel Hill, NC 27599

Edited by Tanya T. Paull, University of Texas, Austin, TX, and accepted by the Editorial Board April 9, 2015 (received for review October 20, 2014)

Nonhomologous end-joining (NHEJ) is a major repair pathway for DNA double-strand breaks (DSBs), involving synapsis and ligation of the broken strands. We describe the use of in vivo and in vitro single-molecule methods to define the organization and interaction of NHEJ repair proteins at DSB ends. Super-resolution fluorescence microscopy allowed the precise visualization of XRCC4, XLF, and DNA ligase IV filaments adjacent to DSBs, which bridge the broken chromosome and direct rejoining. We show, by single-molecule FRET analysis of the Ku/XRCC4/XLF/DNA ligase IV NHEJ ligation complex, that end-to-end synapsis involves a dynamic positioning of the two ends relative to one another. Our observations form the basis of a new model for NHEJ that describes the mechanism whereby filament-forming proteins bridge DNA DSBs in vivo. In this scheme, the filaments at either end of the DSB interact dynamically to achieve optimal configuration and end-to-end positioning and ligation.

genomic integrity | DNA repair | nonhomologous end-joining | super-resolution microscopy | single-molecule FRET

Chromosomal double-strand breaks (DSBs), considered the most cytotoxic form of DNA damage, occur as a result of normal cellular processes (1, 2) as well as cancer therapies (3–5). The cellular DNA damage response (DDR) and repair pathways responsible for maintaining genomic integrity are highly regulated and synchronized processes, both temporally and spatially, involving the coordinated recruitment, assembly, and disassembly of numerous macromolecular complexes (6, 7). In mammalian cells, nonhomologous end-joining (NHEJ) is the primary DSB repair pathway; it is active throughout the cell cycle and is crucial for viability. Dysfunctional NHEJ is associated with several clinical conditions, including LIG4 syndrome and severe combined immunodeficiency (1, 8). Despite its importance, however, the details of how the NHEJ complex assembles at DSBs, brings together a pair of breaks, and organizes subsequent catalytic repair steps remain unknown.

In NHEJ, DSBs are initially recognized by the Ku 70/80 heterodimer (Ku), which encircles dsDNA ends (Ku:DNA) and serves as a molecular scaffold for recruitment of DNA-dependent protein kinase catalytic subunit (DNA-PKcs), XRCC4 (X-ray repair cross-complementing protein 4), XLF (XRCC4 like factor), and DNA ligase IV (LigIV) (1, 9–14). Previous NHEJ models suggested that after binding of Ku to DNA ends, DNA-PKcs binds Ku:DNA to form a DNA-PK holoenzyme and bridges the broken ends (15–18); however, recent experiments indicate that DNA-PKcs may have different roles in NHEJ, such as the stabilization of core NHEJ factors, recruitment and retention of accessory factors, involvement in the DDR signaling cascade, and repair of complex and clustered DSBs (19–25). In addition, recent structural studies have shown that XRCC4 and XLF form filamentous structures in vitro (26–28). Whether such filaments mediate repair in vivo has not yet been determined.

Our present understanding of the cellular NHEJ response to DSBs is based primarily on in vitro biochemical and structural studies done with purified proteins, together with cellular observations in which a radiologic or pharmacologic stimulus damages DNA, allowing observation of the repair process (29–31). Typically, cellular assays rely on a microscope to read out the response, looking for colocalization of DSB repair proteins with large DDR foci; however, conventional microscopy methods allow for only an inferential approach, given that the resolution limit of light is two orders of magnitude greater than the length scale of proteins. Here we used super-resolution (SR) localization microscopy and single-molecule FRET (smFRET) to analyze the cellular organization of NHEJ proteins and define the dynamics associated with end joining in vitro. SR microscopy circumvents the conventional resolution limit of light microscopy by temporally separating emitting fluorophores and computationally fitting the location of each below the diffraction limit. Reconstructing thousands of points in this manner generates an image with a resolution typically an order of magnitude better that that of conventional microscopy (32–34). In addition to this approach, we used smFRET, a powerful method capable of monitoring the dynamics of individual nucleoprotein complexes in real time (35).

Using SR microscopy, we identified previously uncharacterized repair intermediates formed at DSBs in which Ku resides

Significance

Nonhomologous end-joining (NHEJ) is the main pathway for repair of DNA double-strand breaks (DSBs), the most cytotoxic form of DNA damage resulting from ionizing radiation, chemotherapeutics, and normal cellular processes. The mechanisms that control NHEJ play key roles in development, in immunity, and in response to cancer therapy; however, the current state of knowledge regarding the physical nature of the NHEJ repair process is limited. Here we used super-resolution microscopy to define the organization of NHEJ complexes in cells, showing that long filaments form at either side of the break. Single-molecule FRET revealed dynamic behavior in which breaks can pair in an adjacent, non–end-to-end configuration.

Author contributions: D. A. Reid and E.R. designed research; D. A. Reid performed research; D. A. Reid, S.K., G.W., N.T.S., H.H.C., B.A.O., D.F., M.R.L., and D. A. Ramsden contributed new reagents/analytic tools; D. A. Reid, S.K., A.L.-M., D.F., and E.R. analyzed data; and D. A. Reid, M.R.L., D. A. Ramsden, and E.R. wrote the paper.

The authors declare no conflict of interest.

This article is a PNAS Direct Submission. T.T.P. is a Guest Editor invited by the Editorial Board.

[1]To whom correspondence should be addressed. Email: eli.rothenberg@nyumc.org.

This article contains supporting information online at www.pnas.org/lookup/suppl/doi:10.1073/pnas.1420115112/-/DCSupplemental.

at the break site and XRCC4, XLF, and LigIV form long filamentous structures around and over DSB sites. We categorized these intermediates into two different structural subtypes, and defined their kinetics and the structural transitions that occur during the progression of repair. We further verified the formation of these structures using SR imaging analysis of NHEJ reactions carried out in vitro with recombinant proteins. Finally, we used smFRET to characterize the dynamics of end-joining in vitro, revealing that XRCC4/XLF/LigIV mediates end synapsis, and that after initial pairing, the DNA ends undergo dynamic interactions. Our findings identify XRCC4/XLF/LigIV filaments forming on either side of the break and then merging as a key step in DSB repair via NHEJ, and provide a detailed mechanism that is radically different from current models of NHEJ.

Results

SR Imaging Characterizes NHEJ Repair Intermediates in Vivo. We used SR fluorescence localization microscopy (36) to define the molecular architecture of NHEJ protein organization following DNA damage. We induced DSBs in human osteosarcoma cells (U2OS) with the radiomimetic agent bleomycin. The resulting nanoscale-resolved images reveal specific structural and organizational aspects of the size of the protein-DNA complex cluster, contours, and interactions of specific proteins that cannot be obtained via diffraction-limited imaging. To determine the organization of NHEJ proteins with respect to DSB sites, we initially established the localization of cellular DSB sites using a modified TUNEL staining protocol to specifically label free DNA ends (Fig. S1 *A–C*). We then used the TUNEL foci as markers to determine the association of Ku with DSB sites. Owing to its high nuclear abundance, Ku presents a challenge for imaging with conventional approaches (37); however, our SR imaging allows the stochastic activation and imaging of subpopulations of Ku. In contrast to the blurred features observed in the diffraction-limited images, the association of Ku with DSBs marked by TUNEL is clearly resolvable in SR images (Fig. 1*A*). This assay enabled us to accurately detect the formation DSBs after bleomycin treatment, and to monitor their gradual repair (Fig. 1*B*). Quantification of the localization of Ku at DSB sites revealed that Ku occupies >80% of DSB sites both at the basal level and in bleomycin-treated cells (Fig. S1*D*). We also examined Ku/γH2AX to verify the formation of DSBs and progression of DDR, and found a significant increase in overlaps between the two proteins in damaged cells (Fig. S1 *E* and *F*).

To determine the spatial organization of the NHEJ machinery, we examined the associations of the components of the NHEJ ligation complex, XRCC4, XLF, and LigIV, with Ku and with DSB sites marked by TUNEL. Antibodies for immunofluorescence were validated in U2OS cells after treatment of cells with siRNAs specific to XRCC4, XLF, or LigIV (Fig. S2 *A* and *B* and Table S1). Formation of NHEJ repair complexes after the induction of DSBs by bleomycin was evident, with a significant increase in the overlap of key NHEJ factors Ku/XLF, Ku/LigIV, and LigIV/XRCC4 (Fig. 1*C*). Several recent in vitro studies

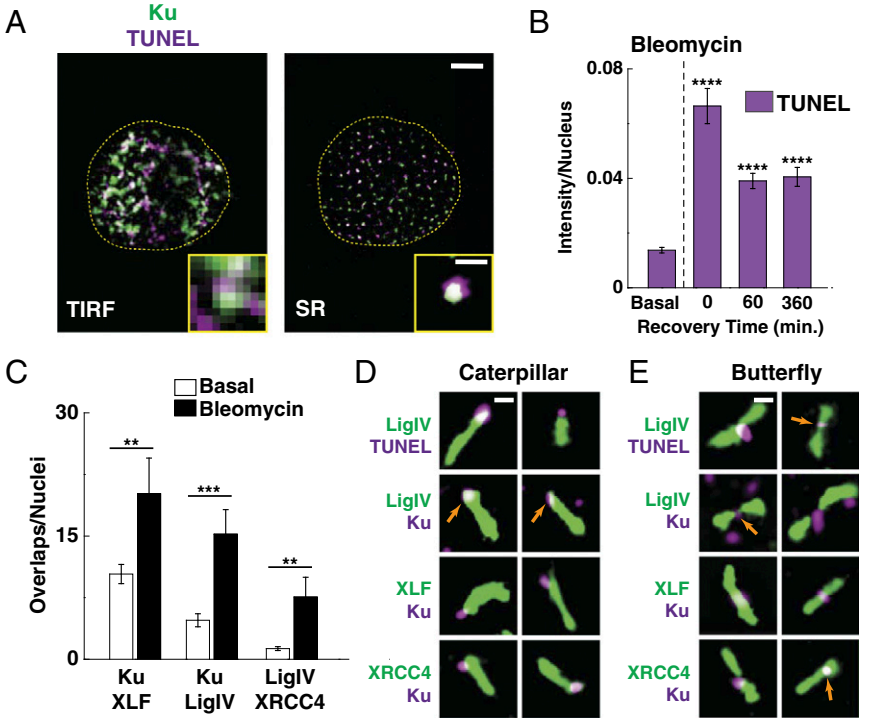

Fig. 1. Organization of NHEJ proteins in response to DNA damage. (*A*) Representative nuclei (dashed yellow line) stained for Ku/TUNEL displayed with conventional resolution microscopy (TIRF) and reconstructed SR microscopy. (*Inset*) Zoomed region in which Ku associates with a DNA break marked by TUNEL. (Scale bars: 5 μm and 500 nm, respectively.) (*B*) Quantification of DNA breaks measured over the course of 6 h by observing the normalized stained area of TUNEL foci (area of TUNEL particles/nuclear area). The amount of TUNEL staining increases rapidly after DNA damage, but decreases as repairs occur. Number of cells, $n = 39$, 14, 14, and 16, respectively. (*C*) Quantification of the association between various NHEJ proteins at the basal level and after bleomycin treatment. The number of interactions/nuclei increases after damage. Number of cells, $n = 63/12$, 27/17, and 20/19, respectively. (*D*) Repair structures (Caterpillars) from cells in which NHEJ filament proteins interact with a DSB. LigIV/TUNEL shows a long filament capped by a DSB (orange arrows). These structures are observable using Ku and XRCC4/XLF/LigIV. (Scale bar: 250 nm.) (*E*) Repair structures (Butterflies) from cells showing NHEJ filament proteins interacting with a DSB. LigIV/TUNEL shows DSB (orange arrow) roughly near the filament center of mass. These structures are observable using Ku and XRCC4/XLF/LigIV. In this class of structure, we identified two characteristic subtypes; in the first, gapped filaments are separated by a cluster of Ku, whereas in the second, we found continuous filaments with Ku at their center. (Scale bar: 250 nm.) Error bars represent SEM. $^{**}P < 0.01$; $^{***}P < 0.001$; $^{****}P < 0.0001$.

have shown that XLF and XRCC4 form extended filaments (26, 27, 38–42). Importantly, our SR imaging revealed that XRCC4 and XLF filaments exist in vivo, and also that LigIV appears to form filamentous structures in cells (Fig. S2*C*).

LigIV is thought to modulate the oligimerization of XRCC4, raising the question as to whether its absence will ablate filament formation. We treated cells with siRNA for LigIV and still found filaments containing XRCC4 and XLF, implying that LigIV is dispensable for filament formation (Fig. S2*D*). Quantification of the physical parameters (length, width, perimeter, and area) of LigIV clusters shows a distinct difference in their distributions, where LigIV complexes that interact with Ku exhibit a shift to larger values compared with LigIV complexes that do not interact with Ku (Fig. S3 *A* and *B*). This indicates that the organization of LigIV complexes is modulated when recruited to DSBs.

In-depth analysis of the structures formed by LigIV at DSBs sites (LigIV/TUNEL overlap) revealed spatially organized complexes in which TUNEL staining either caps or is centered within elongated filaments of LigIV (Fig. 1 *D* and *E*). Similar structures were observed for Ku/LigIV, Ku/XLF, and Ku/XRCC4 complexes (Fig. 1 *D* and *E*). For clarity, we classified the Ku/DSB capped structures (Fig. 1*D*) as caterpillar-shaped ("Caterpillars"), and complexes showing Ku/DSB near the midpoint of the filament containing structure as butterfly-shaped ("Butterflies") (Fig. 1*E* and Fig. S3*C*). To verify the dependence of these structures on the NHEJ filament-forming factors, we imaged cells treated with siRNAs targeting XRCC4, XLF, and LigIV. Cells treated with siRNAs to knock down filament proteins showed a significant decrease in the relative frequency of both Ku/LigIV Butterfly and Caterpillar structures compared with control siRNA-treated cells (Fig. S4 *A* and *B*). In addition, cells treated with the DNA-PKcs inhibitor NU7441 showed a decrease in both structures, although not as pronounced as in the case of cells treated with siRNAs targeting the filament proteins (Fig. S4 *C* and *D*).

In Vitro Reconstitution of Repair Intermediates. To further verify the formation of the repair structures observed in vivo, we developed an assay to recapitulate the NHEJ structures in vitro using recombinant NHEJ proteins and dsDNA. In this assay (illustrated in Fig. 2*A* and detailed in *Methods*), NHEJ proteins were incubated with linearized plasmid dsDNA, allowing assembly of NHEJ proteins on the DNA, facilitating NHEJ and formation of intermediates in that pathway. This reaction was performed in the absence or presence of the LigIV-specific inhibitor SCR7 (43). A cross-linking reagent [4% (wt/vol) paraformaldehyde (PFA)] was then added to the reactions to preserve structural intermediates. The resulting cross-linked nucleoprotein complexes were adsorbed onto a silanized coverslip surface, followed by immunofluorescence staining and SR imaging. To confirm that the resulting complexes are indeed due to the NHEJ reaction and to rule out labeling artifacts, we performed the same reaction in the presence of DNA only (i.e., without additional proteins) and proteins only (i.e., no DNA). The DNA-only control did not yield any filaments or structures, as expected. In our assay, XRCC4 and LX (copurified LigIV/XRCC4) were capable of forming filaments (Fig. S5 *A* and *B*), consistent with

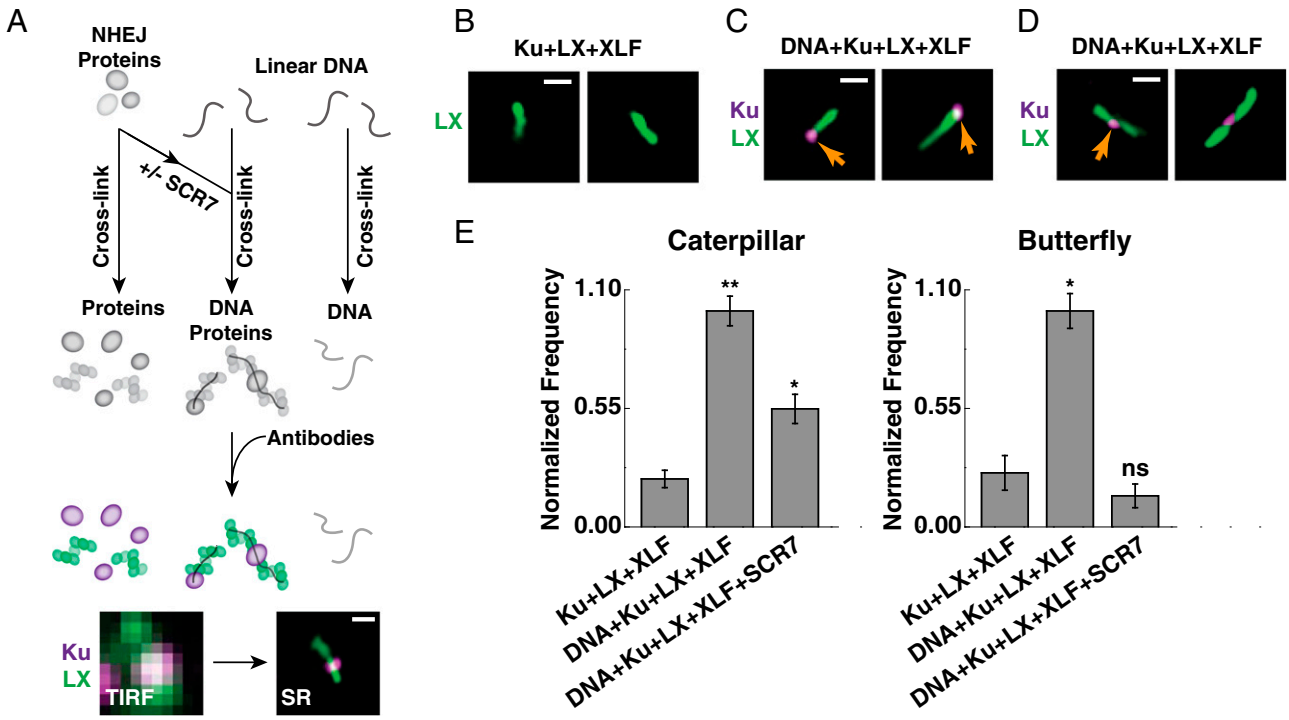

Fig. 2. NHEJ proteins form structures in vitro. (*A*) (*Upper*) Cartoon showing the assembly procedure used to reconstitute NHEJ repair structures for in vitro SR imaging. DNA, protein, and DNA with proteins were reacted for 30 min and then cross-linked. Subsequently, they were bound to a coverslip, immunofluorescently labeled, and imaged as in our cellular SR assay. (*Lower*) Comparison of the regular diffraction limited microscopy image showing blurred features and a reconstructed SR image, in which the nanoscale organization and features of NHEJ DDR intermediates are clearly shown. (Scale bar: 250 nm.) (*B*) Observation of LX filaments formed in the absence of DNA. NHEJ proteins (6 μM Ku, LX, and XLF) were incubated in the absence of DNA and stained for LigIV and Ku. (Scale bar: 250 nm.) (*C* and *D*) In the presence of DNA, NHEJ proteins (6 μM Ku/LX/XLF) formed two characteristic structures. The first type of structure (Caterpillars) is shown in *C*, where Ku is localized at the end of LX filaments. The second type of structure (Butterflies) is shown in *D*, in which Ku is localized near the center of the LX filaments. Orange arrows illuminate Ku locations. (Scale bar: 250 nm.) (*E*) Quantification of the frequency of Caterpillar and Butterfly structures in our reconstituted reactions, showing that the formation of the observed structures is highly reliant on DNA. The addition of 100 μM SCR7 resulted in a decrease in Butterfly structures. The abundance of each structure is normalized to the amount present in the DNA, Ku, LX, and XLF reactions. Error bars represent SEM. ns, *P* value not significant; $*P < 0.05$; $**P < 0.001$.

previous reports that XLF/XRCC4 can form filaments in the absence of DNA (41). When the proteins Ku, LX, and XLF were reacted, we observed similar filaments when staining for LigIV (Fig. 2*B*), in agreement with our observation that LigIV can form elongated structures in vivo without the induction of external damage.

The products of NHEJ reactions containing DNA, Ku, LX, and XLF are shown in Fig. 2 *C* and *D*. Specifically, we found the products thus generated display long LigIV-containing filaments that are either capped or interrupted by Ku foci—visually similar to the Caterpillar or Butterfly structures that we characterized in cells. In addition to these structures, we also observed structures in which Ku is localized on both ends (two-headed Caterpillars) and structures linked in series (joined Butterflies) (Fig. S5 *C* and *D*). Omitting DNA from the reactions resulted in a significant decrease in both structures, whereas adding the LigIV inhibitor SCR7 resulted in a significant decrease in the number of Butterflies (Fig. 2*E*).

We also examined how XLF and XRCC4 affect the reaction products. Eliminating XLF from the reaction resulted in a significant decrease in the number of both Caterpillar and Butterfly structures, whereas supplementation with XRCC4 resulted in a reduction in Caterpillar structures, but no statistically significant change in the number of Butterfly structures (Fig. S5*E*). Replacing magnesium with calcium in our reaction buffer resulted in a sharp decrease in both Butterfly and Caterpillar structures, similar to treatment with SCR7. Finally, removal of the 5′ phosphate from the DNA resulted in no change in the number of Caterpillar structures and a decrease in the number of Butterfly structures (Fig. S5*E*). Quantification of the mean length of LX filaments in the different reactions revealed that LX forms longer filaments in the presence of DNA, with lengths comparable to those of digested plasmid DNA (Fig. S5*F*). Overall, the structures obtained from our reconstituted in vitro assays are visually consistent with our findings of Caterpillar and Butterfly structures observed in vivo, and formally demonstrate that the structures observed in cells are indeed repair intermediates. Moreover, our assay also demonstrates that Ku/LX/XLF proteins together constitute a sufficient system for generating these structures in vitro.

Particle Averaging of NHEJ Structures. We further characterized the observed structures in cells using dual-color single-particle averaging. For each particle, the two color channels were separated, followed by alignment, averaging, and recombination of the images (Fig. S6 *A*–*D*). Whereas the Caterpillar structure could not be easily separated into further classes, the Butterfly structures could be readily subdivided into two subclasses based on whether they were a single "continuous" filament or two adjoining filaments separated by Ku; we term the latter structure a "gapped" filament. The resulting particle averages of Caterpillars, continuous Butterflies, and gapped Butterflies, shown in Fig. 3 *A*–*C*, define novel DDR intermediates in the NHEJ pathway. These structures show the organizational tendencies of NHEJ repair intermediates. The Caterpillar structure is a single DSB to which Ku is bound, thus recruiting a filament containing XRCC4, XLF, and LigIV, whereas the Butterfly structure represents end-to-end synapses of two DSBs.

Structural Kinetics of Repair Intermediates. To determine the context of the observed Butterfly and Caterpillar structures in the DSB repair pathway, we monitored their accumulation and dissolution after induction of cellular damage. A small number of

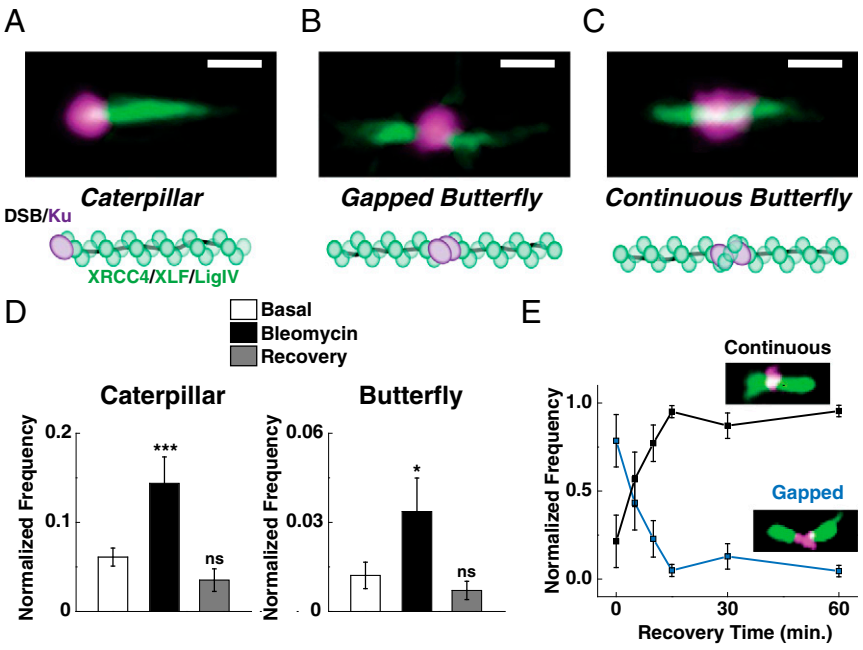

Fig. 3. Particle averaging of repair intermediates and kinetic analysis. (*A*–*C*) Representative average particle obtained for each of the three categories: Caterpillar ($n = 42$) (*A*), gapped Butterfly ($n = 42$) (*B*), and continuous Butterfly ($n = 20$) (*C*). (Scale bar: 250 nm.) Illustrations of the three types of observed structures are below the particle average image. (*D*) Quantification of the relative abundance of LigIV Caterpillar and Butterfly structures in untreated cells (basal), following bleomycin treatment, taken between 0–60 min (bleomycin), and a further recovery time point at 360 min (recovery). Structures were normalized to the total number of interacting particles in each cell. Number of cells, $n = 27$, 100, and 21, respectively. (*E*) Kinetics of Butterfly structures during repair. The two different Butterfly structures were monitored after 5 min of bleomycin-induced damage. Gapped Butterflies (blue squares) and continuous Butterflies (black squares) are shown as a function of DSB recovery time. These populations were strongly anticorrelated in time, with gapped filaments decreasing sharply within 15 min of recovery time and continuous filaments increasing within 15 min. This analysis shows that the gapped structures are most abundant immediately after DSB induction. With increased recovery time, the predominant population becomes continuous Butterflies. Number of cells, $n =$ 13, 17, 8, 19, 27, and 16, respectively, with $n = 119$ structures examined. Error bars represent SEM. ns, *P* value not significant; $^*P < 0.05$; $^{***}P < 0.001$.

these structures were observed in cells owing to a basal-level DDR in the absence of damaging agents. After treatment of cells with bleomycin, we observed a significant increase in their occurrence within the next hour, followed by a decrease back to basal levels by 6 h after treatment (Fig. 3*D*). Notably, more Caterpillar structures than Butterfly structures were seen both at the basal level and after DSB induction; this may reflect persistent unpaired breaks or partially disassembled Butterfly structures after repair. We speculate that unpaired breaks may arise from the complexity of the break and/or proximity to chromatin structures that prohibit the assembly of filaments. Kinetic analysis of the presence of gapped and continuous Butterfly subpopulations after DSB induction showed a reciprocal relationship, in which the continuous subpopulation increased sharply in the first 15 min of recovery, whereas the gapped species showed the opposite response (Fig. 3*E*). These data are reminiscent of previous analyses of the kinetics of DSB repair by NHEJ in which a fraction of lesions was repaired in less than 30 min (44, 45); thus, continuous filaments likely represent fully rejoined DSBs before dissociation of the NHEJ complex (Fig. S6*E*).

Real-Time smFRET Analysis of the End-Joining Reaction. To investigate the dynamics of the end-joining process, we monitored the synapsis of the two ends in real time using an smFRET assay (Fig. 4*A*). This dsDNA capture assay is based on a long (~80 bp) dsDNA substrate with complementary four nucleotide overhangs labeled with the FRET acceptor fluorophore, which is tethered to the surface of a perfusion chamber, and a donor-labeled dsDNA substrate, which is added along with the NHEJ proteins (oligonucleotide sequences are detailed in Table S2). Because only donor-labeled dsDNA molecules are directly excited, no signal is produced unless the incoming donor dsDNA attaches to the surface-bound acceptor dsDNA, thereby directly probing synapsis and end-joining. The donor and acceptor dsDNA substrates were designed to have only one end accessible for loading of Ku, end-joining, and ligation (Fig. 4*A*). Specifically, one of the ends of the donor substrate was blocked with a closed stem loop structure that was sufficient to prevent loading of Ku (Fig. S7*A*), and one of the ends of the acceptor substrate was biotinylated directly to a neutravidin-covered PEG surface, occluding loading and ligation of that end (46). By positioning the donor (green) and acceptor (red) FRET pair at the accessible ends of incoming and surface-bound dsDNA, respectively, this experiment allowed us to directly monitor the end-to-end distance changes during synapsis and end-joining.

We established which NHEJ proteins are required for effective synapsis and end-joining. The concentrations of surface-bound acceptor dsDNA and incoming donor-dsDNA were kept fixed (250 pM and 1 nM, respectively), and the protein concentrations and ratios were changed to generate optimal end-joining. The efficiency was quantified as the number of resulting donor/acceptor FRET pairs observed immediately after the addition of NHEJ proteins and donor dsDNA substrate to the perfusion chamber. Fig. 4*B* and Fig. S7*B* show representative images of individual donor/acceptor molecule pairs after the addition of different NHEJ proteins and donor-labeled dsDNA, and quantification of their end-bridging efficiency is illustrated in Fig. 4*C*. We found that LX/XLF supports synapsis, but the presence of Ku in the complex (Ku/LX and Ku/LX/XLF) stimulates greater synapsis. The addition of DNA-PKcs with either Ku or Ku/LX/XLF did not increase the number of individual complexes, but resulted in large foci indicative of multiple paired donor complexes (visible in Fig. 4*B*). The observation of large foci mediated by DNA-PKcs is in agreement with recent studies showing that DNA-PKcs facilitates the aggregated joining of multiple DNA breaks, playing a role in the repair of clustered DSBs rather than simple DSBs (23, 47, 48). Thus, these findings specifically identify Ku/LX/XLF as the core complex required to mediate synapsis and productive end-joining.

To determine the positioning of the two dsDNA ends during the end-joining process, we compared an smFRET population histogram of dsDNA molecules actively undergoing synapsis and ligation with a histogram of fully ligated dsDNA molecules (Fig. 5*A*). These histograms were generated by measuring the FRET signal either immediately after initiation of the NHEJ reaction by the addition of Ku/LX/XLF along the donor strand, or after purification of ligated molecules by a high-salt buffer (1 M NaCl) wash of bound DNA complexes after an additional 15-min incubation.

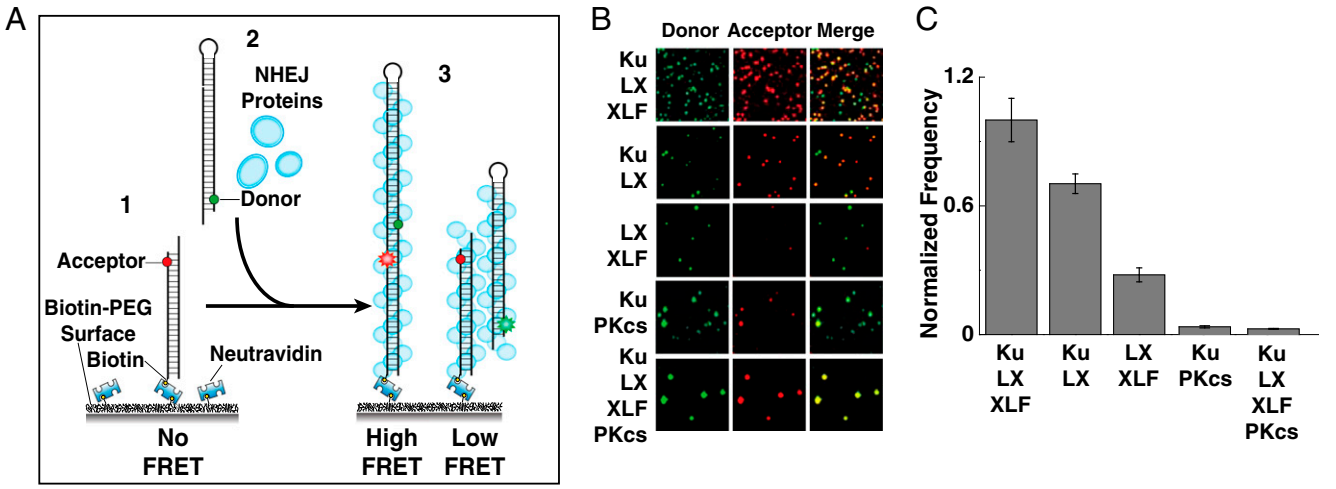

Fig. 4. smFRET of NHEJ synapsis and ligation. (*A*) Diagram illustrating our NHEJ smFRET dsDNA capture assay. (1) dsDNA with four nucleotides of ssDNA and an acceptor dye bound to the surface. (2) Solution containing various NHEJ proteins and a dsDNA with a complementary four-nucleotide overhang labeled with a donor dye is added into the chamber. (3) Pairing between the two dsDNAs occurs, and FRET is observed. (*B*) Images from the smFRET synapsis reaction showing donor/acceptor channels for different combinations of NHEJ factors. Spots represent individual pairs of DNA molecules. Ku/LX/XLF showed the most abundant pairing, whereas reactions containing DNA-PKcs resulted in formation of large aggregates of the solution DNA strand. (*C*) Quantification of synapsis as a function of NHEJ proteins added using an smFRET dsDNA capture assay. Although some stable synapsis is observed for LX/XLF, synapsis improves with the addition of Ku, as seen in Ku/XLF and Ku/LX/XLF. Pairing efficiency is normalized to the reaction containing Ku/LX/XLF. Number of observed FRET pairs, n >1,000 molecules. Error bars represent SEM.

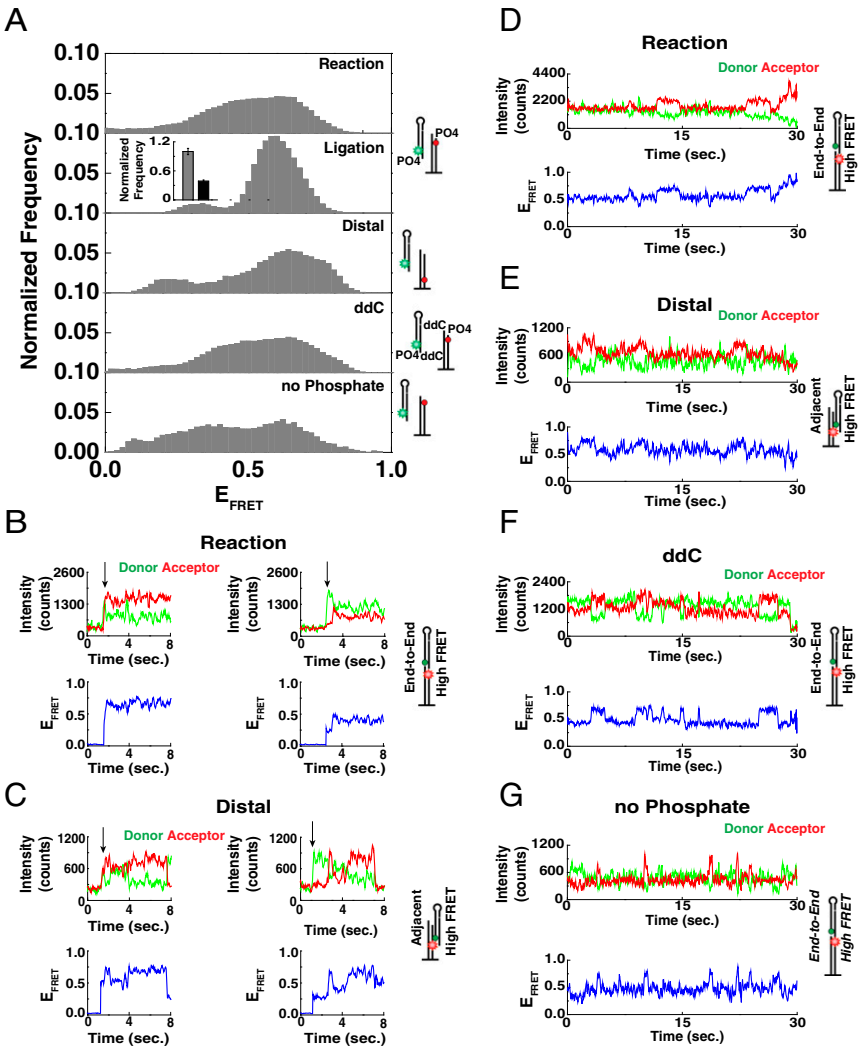

Fig. 5. Kinetic analysis of NHEJ dynamics with smFRET. (*A*) FRET histograms of the synaptic complex (50 nM Ku/LX/XLF) during ligation reactions showing a broad distribution of FRET values. The Reaction panel is a substrate with a 5′ phosphate capable of undergoing ligation. The Ligation panel is the remaining population from the Reaction panel following a 1 M NaCl wash. (*Inset*) Comparison of the normalized number of molecules (Reaction) and following the salt wash (Ligation), in which the effective yield of the ligation was calculated to be ∼38% of FRET pairs seen in the reaction. The Distal panel shows a substrate in which the acceptor was placed ∼60 bp from the DNA end. The ddC panel shows a substrate in which ligation is blocked by dideoxy nucleotides on the 3′ ends. The no Phosphate panel shows a substrate that lacks 5′ phosphate and is unable to complete ligation. Each pair of substrates has complementary four nucleotide overhangs. All histograms show broad distributions of FRET values. Number of observed FRET pairs, n = 200, 200, 68, 200, and 100 molecules, respectively. (*B*) Two representative smFRET trajectories showing the initial NHEJ pairing of the two dsDNA strands at a high-FRET state (*Left*) and a low-FRET state (*Right*), demonstrating that initial pairing occurs at both end-to-end and adjacent configurations, as illustrated in the cartoons on the right. The reaction was carried out with 50 nM Ku/LX/XLF. (*C*) Two representative smFRET trajectories for surface dsDNA with distal acceptor dye. Initial pairing of the two dsDNA strands occurs at either a high-FRET state (*Left*) or a low-FRET state (*Right*), further demonstrating that initial pairings occur at both end-to-end and adjacent configurations, as illustrated in the cartoons on the right. The reactions were carried out with 50 nM Ku/LX/XLF. The trajectories exhibit well-defined FRET values and limited fluctuations, consistent with stably ligated dsDNA. (*D*) Representative smFRET trajectories showing repetitive transitions of a paired synaptic complex between adjacent and end-to-end configurations. (*E*) Representative smFRET trajectories showing fast transitions during synapsis for distal acceptor surface dsDNA. These trajectories resembles those in which the dye is placed close to the accessible DNA end showing repetitive transitions between adjacent configurations and end-to-end configurations. (*F*) Representative smFRET trajectories showing fast transitions during synapsis for ddC substrates. These trajectories resemble those in which the dye is placed close to the accessible DNA end (as in Fig. 5*E*), showing repetitive transitions between adjacent configurations and end-to-end configurations. (*G*) Representative smFRET trajectories showing fast transitions during synapsis for substrates with no phosphate. These trajectories resemble those in which the dye is placed close to the accessible DNA end (as in Fig. 5*E*), showing repetitive transitions between adjacent and end-to-end configurations. Error bars represent SEM.

The histogram for complexes formed during synapsis (Fig. 5*A*, Reaction) shows a broad distribution (FWHM ∼0.3) centered at FRET ∼0.55, whereas after the salt buffer wash (Fig. 5*A*, Ligation), the FRET histogram narrows to a width of FWHM ∼0.15 around the center of FRET ∼0.65. The FRET values after buffer wash are in agreement with the expected FRET value in which the FRET pair is located in a fully ligated dsDNA (4.3 nm; FRET ∼0.65). The broadening observed immediately after addition of the ligation complex implies dynamic processes associated with initial synapsis of the two ends. Quantification of the mean number of complexes per imaging area exhibiting FRET interaction during the NHEJ reaction and postligation following the high-salt buffer wash is shown in the Inset of Fig. 5*A*, Ligation. This analysis revealed that ∼60% of the molecules that form synaptic complexes during the NHEJ reaction are not ligated within the reaction time, and dissociate after the high-salt wash.

To further probe the pairing step of NHEJ, we examined synapsis in additional substrates that are unable to undergo ligation (i.e., dideoxy 3′ ends or lacking 5′ phosphates) (Fig. S8*A*). We used two substrates lacking 5′ phosphate, with the acceptor dye positioned either at the free DNA end (no Phosphate) or at ∼60 bp from the free DNA end (Distal). Pairing in these substrates resulted in smFRET histograms with similar broad distributions (Fig. 5*A*, Distal). Importantly, the wide FRET distribution, along with high FRET states observed in the distal acceptor substrate, indicate that the DNA substrate may be interacting in an adjacent configuration. A similar FRET distribution was obtained for a substrate with 5′ phosphates but blocked for ligation with dideoxy at 3′ ends (Fig. 5*A*, ddC), indicative of a ligation-independent pairing process. To verify these observations, we also carried out an NHEJ reaction in the presence of the LigIV inhibitor SCR7 with the ligatable substrates shown in Fig. 5*A*, which showed only a slight reduction in pairing efficiency, although ligation was prohibited (Fig. S8 *B* and *C*). Taken together, these findings identify an initial NHEJ pairing process that is distinct from the end-ligation step.

Dynamics of NHEJ Ligation Complex. To characterize the dynamics of end-to-end positioning, we examined individual smFRET trajectories obtained immediately after initiation of the NHEJ reaction. Fig. 5*B* shows two representative trajectories that demonstrate the initial encounter between the two ends (denoted by an arrow). In this experiment, a signal was observed only after arrival of the donor dsDNA (Fig. 5*B*, *Left*: t = 2 s, *Right*: t = 3 s). The two trajectories shown in Fig. 5*B* differ in their pairing configuration during initial encounter; the one on the left shows an initial encounter at a high FRET, followed by dynamic fluctuations in the FRET signal, whereas that on the right shows an initial encounter at low FRET, followed by an increase to intermediate FRET. The variation in the initial encounter FRET values along with the width in the FRET histogram in Fig. 5*A* shows that the initial pairing configuration is likely to be such that the ends are positioned not in an end-to-end configuration, but rather away from each another, as illustrated in the cartoons shown next to the trajectories. This conclusion is further supported by our quantification of the initial FRET value and change in FRET values after initial binding (Fig. S8*D*).

To further validate that the initial encounter can occur when the dsDNAs are in an adjacent configuration with the ends positioned away from one another, we examined initial pairing trajectories from the distal acceptor substrates. In this FRET configuration, high FRET would result only when the two dsDNA substrates were paired in an adjacent configuration. With these FRET substrates, we observed initial pairing trajectories displaying high FRET values with dynamic fluctuations (Fig. 5*C*). To exclude the possibility that these high FRET values stem from the donor-labeled end of the free dsDNA substrate randomly engaging with immobilized DNA, we used two additional free dsDNA substrates that were labeled farther away from the free end (Fig. S8 *E*–*I*). These substrates were reacted with either end-labeled or internally/distal-labeled surface- immobilized dsDNA. These reactions exhibited broad distributions of FRET values spanning both high and low FRET values. Notably, high FRET values were detected even for substrates in which both the free dsDNA and the surface-immobilized dsDNA are labeled away from their accessible ends. Thus, the observed behavior is not likely to be a result of random interaction with the free dsDNA end. Taken together, these observations establish that the two ends can be paired in an adjacent configuration in which the two ends are situated away from each another while undergoing dynamic end-to-end rearrangements.

We next examined whether the observed dynamic repositioning of the ends stems from the initial pairing configuration or occurs throughout the NHEJ process. To determine this, we analyzed smFRET trajectories obtained for the substrates shown in Fig. 5*A* (Reaction), donor/acceptor substrates that are already paired but not ligated and do not demonstrate initial encounter events. Unlike fully ligated molecules that exhibit steady FRET values throughout the trajectory (Fig. S8*J*), these trajectories displayed rapid transitions in FRET values (Fig. 5*E*). We infer that the dynamics observed are characteristic of NHEJ pairing interactions and are not a direct consequence of the initial encounter event. Similar dynamic transitions were observed for the distal acceptor substrate and the ddC substrate blocking ligation, as well as the substrate without phosphate (Fig. 5 *F* and *G*). These dynamics, along with the broad FRET populations, are consistent with multiple adjacent pairing configurations afforded by the long XRCC4/XLF/LigIV filaments. In such a scheme, dynamic transitions between these configurations result in proper positioning of the paired ends. We note that the adjacent configuration that we describe is broadly termed and refers to the various modes of interaction between adjacent filaments, including a range of configurations in which the filaments are not strictly parallel or are antiparallel.

Discussion

In the work reported here, we used an array of single-molecule methods to define the organization, dynamics, and kinetics of NHEJ proteins in vitro and in vivo. Using SR microscopy, we resolved the organization of NHEJ proteins and identified previously unknown NHEJ-specific repair structures (Fig. 1). Using an in vitro SR assay with recombinant NHEJ proteins, we further established the structures of the repair intermediates that we observed in cells (Figs. 2 and 3), which enabled us to define a minimal system for their assembly in vitro. Using smFRET analysis, we dissected the initial steps of the end-joining process and associated dynamics and showed that XRCC4/XLF/LigIV complexes mediate pairing of dsDNA ends (Figs. 4 and 5). Our findings thus provide crucial new insights into the mechanism of DNA DSB repair via NHEJ.

The formation of XRCC4 and XLF filaments has been shown to occur in vitro, posing fundamental questions regarding the roles of these filaments, particularly in vivo (27, 28). Moreover, the involvement of LigIV with these structures was uncertain (26). Our discovery that filaments do indeed form in cells, and that these localize to DSB sites, sheds new light on the physical organization of the NHEJ repair complex (Fig. 1). Taken together, these observations explain how the broken ends are maintained in the same complex, and how LigIV arrives at the break site after pairing. The formation of long filaments capable of interacting with one another at either side of the break enables multiple pairing configurations, thereby increasing the pairing probability of the two ends. Once initial pairing is achieved, the interaction between nucleoprotein complexes at either side of the break maintains the broken ends together while they are processed for ligation. Given that XRCC4 is approximately three times more abundant than LigIV, and that the two proteins persist in a heterodimer form of XRCC4/LigIV, it is likely that all LigIV is bound by XRCC4, such that XRCC4/XLF and XRCC4/LigIV form interwoven filaments (49). Importantly, based on our kinetic analysis, we conclude that these filaments are capable of dynamic rearrangement around the break site during the progression of repair (Fig. 3).

An understanding of the initial steps that occur after a DSB break but before ligation is of fundamental importance. Much of what we currently know about the temporal dynamics of NHEJ proteins in DSBs relies on time-resolved microscopy experiments using fluorescent-tagged NHEJ components (12, 19, 37, 50); however, none of those studies addressed issues relating to positioning of the ends and the repair machinery during synapsis or the dynamics associated with the repair process before ligation. Specifically, it is not known how the broken ends are brought

together, with respect to either their initial pairing configurations or the nature of the pairing interaction. Our smFRET analysis provides critical mechanistic insight into these processes. We show that initial pairing can occur in different configurations, both end-to-end and adjacent, and that the synaptic complex can stay bound together while dynamically and continually transitioning between end-to-end and adjacent configurations (Fig. 5). This provides a platform for continually repositioning the two ends while they are being processed. Importantly, the adjacent configuration is consistent with an interaction between XRCC4/XLF/LigIV proteins on each dsDNA strand that is localized away from the ends, as would be anticipated in filaments. Crystal structures of ligases interacting with strand-break substrates indicate that an end-to-end configuration is required for the final step in NHEJ (51, 52). We suggest that the alternate, adjacent configuration that we observed here is critical to allow engagement of ends by processing enzymes (e.g., Artemis). Together with the observed dynamic switching between the two configurations, this allows for repeated cycles of processing and attempted ligation while continuously maintaining synapsis of a given end pair.

Taken together, our findings present a unique picture of the organization and dynamics of the NHEJ system and provide a basis for a new integrated model for DNA DSB repair via the NHEJ pathway (Fig. 6). We propose a model consisting of two distinct kinetic steps, illustrated in Fig. 6: (*i*) pairing of the broken ends and (*ii*) alignment of the ends within the synaptic complex to enable ligation. On formation of a DSB, Ku binds to broken ends, recruiting XRCC4/XLF/LigIV to form filaments on DNA in the vicinity of the break (53–57), resulting in Caterpillar structures. The presence of filaments at either side of the break is advantageous, allowing for more pairing configurations compared with pairing events occurring only at the ends, thereby increasing the probability of pairing. When two Caterpillar structures meet, the XRCC4/XLF/LigIV filaments pair in either a direct end-to-end or an adjacent configuration, forming Butterfly structures (41, 42).

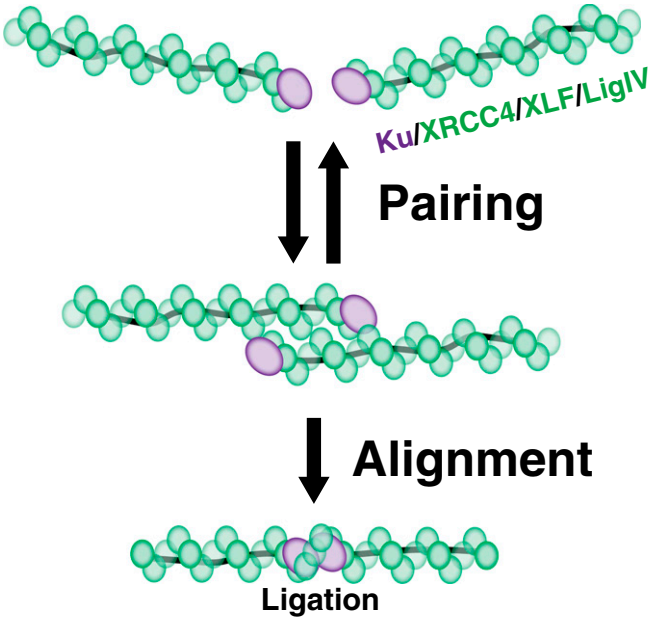

Fig. 6. Model for DSB repair via NHEJ. After Ku loading, XRCC4/XLF/LigIV filaments are recruited, creating Caterpillar structures. Synapsis between two Caterpillar structures commences, such that the structures can align end-to-end, as seen in our SR images. When the two DNA ends are in an end-to-end configuration in which the ends are compatible for ligation, the filament will merge over the two ends to initiate end ligation.

The interaction within the synaptic complex after pairing is dynamic, ensuring that the DSB ends remain together while providing accessibility for accessory factors to process chemically incompatible ends for ligation. Moreover, the alignment of the paired ends within the synaptic complex is beneficial because of the reduced dimensionality of the search process (58). We speculate that the directionality of the alignment process may be mediated by the interaction of Ku with the opposite filament (19, 59). When the DNA ends are properly positioned in a Butterfly structure, the filament will form a continuous bridge across the break. The distribution of LigIV along the filament, together with continual repositioning of the broken ends, allow for appropriate end-to-end configuration and ligation to occur. Finally, we speculate that the association of DNA-PKcs with the Ku/LX/XLF structures may further stabilize these repair intermediates, providing an additional level of regulation and coordination of the NHEJ repair process.

Methods

Cell Culture. U2OS cells (American Type Culture Collection) were cultured as specified by the supplier. Cells were serum-starved for 72 h before DNA damage was induced, to cause cells to be primarily in G1/G0, which is known to favor the NHEJ pathway. Cells were damaged with 50 μg/mL bleomycin for various times either for fixed exposure (0–60 min to monitor accumulated damage) or for a recovery experiment (5 min of exposure, a media wash, and 0–360 min of recovery time) (60). SiRNAs, purchased from Qiagen (Table S2), were transfected into unsynchronized U2OS cells with RNAiMAX Lipofectamine (Life Technologies). Cells were subsequently cultured for 3 d before being harvested, to access RNA interference efficiency with Western blot analyses. DNA-PKcs was inhibited by treating cells with either DMSO or 3 μM NU7441 for 1 h, after which the cells were damaged and fixed.

Western Blot Analysis. Western blot analyses were performed as described previously (61). Antibodies used in these analyses included XRCC4 (HPA006801; Sigma-Aldrich), XLF (NBP2-03275; Novus Biologicals), and DNA ligase IV (ab80514; Abcam).

Immunofluorescence. Cells were washed with PBS and then extracted with cold CSK buffer containing 0.5% Triton X-100 (37), then washed again with PBS and immediately fixed with 4% (wt/vol) PFA for 20 min. Coverslips were blocked with blocking solution [20 mg/mL BSA, 0.2% gelatin, 2% (wt/vol) glycine, 50 mM NH_4Cl, and PBS], then stained with primary antibodies (at dilutions specified by the manufacturer either overnight at 4 °C or for 1 h at room temperature) and secondary antibodies (usually at 1:1,000–5,000 for 30 min at room temperature) in blocking solution before imaging. TUNEL staining was provided with a commercial Click-iT TUNEL Alexa Fluor 647 Imaging Assay (Life Technologies), with the Click-iT reaction performed with the labeling reagents from a Click-iT EdU Alexa Fluor 647 Imaging Assay (Life Technologies), using a 1:100 dye dilution. The following antibodies were used for protein detection: γH2AX JBW301 (MA12022; Thermo Scientific), γH2AX (NB100-384; Novus Biologicals), Ku 70/80 (MS-285-P1; Thermo Scientific), DNA ligase IV (ab80514; Abcam), XLF (ab33499; Abcam), XRCC4 (HPA006801; Sigma-Aldrich), and secondary antibodies conjugated to Alexa Fluor 568 and Alexa Fluor 647 (Life Technologies).

SR Imaging. SR imaging was achieved through a modified assay based on a direct stochastic optical reconstruction microscopy approach, as reported previously (32–34, 62, 63). In brief, buffer containing 100 mM 2-mercaptoethylamine (MEA), 0.8% glucose, and an oxygen-scavenging system (containing 1 mg/mL glucose oxidase and 0.02 mg/mL catalase) was used during image acquisition. Images were acquired on a custom-built TIRF microscope (*SI Materials and Methods*) and reconstructed with the freely available ImageJ QuickPALM plug-in (64).

Protein Purification.

Ku70/86. Purification of Ku70/86 has been described previously (65). In brief, Hi-5 insect cells (B855-02; Invitrogen) were coinfected with baculovirus containing C-terminal His-tagged Ku70 and untagged Ku86. Cells were lysed and purified by Ni-NTA affinity chromatography (Qiagen), DNA affinity chromatography, and MonoQ 5/50 GL anion-exchange chromatography (GE Healthcare). LX (LigIV/XRCC4) and XLF were purified from Hi-5 cells (Life Technologies) overexpressing baculovirus-delivered constructs, and then purified by successive chromatography using first hexahistidine affinity and then anion exchange (Mono Q; GE Healthcare), as described previously (11, 66). DNA-PKcs was purified as described previously (67).

In Vitro SR Imaging Assay. Plasmid DNA (pUC19; New England Biolabs) was digested with BglI to yield two fragments of ~1.1 and 1.5 kb. In vitro NHEJ reactions were carried out in NEB4 buffer (20 mM Tris acetate pH 8.3, 10 mM magnesium acetate, 50 mM potassium acetate, and 2 mM DTT). Then 5–30 nM DNA was reacted with purified proteins at a concentration of 6 μM for Ku, LX, and XLF. The reaction was supplemented with DMSO or 100 μM SCR7 to test inhibition. Removal of the 5′ phosphate was done with recombinant shrimp alkaline phosphatase. The reaction was carried for 30 min at room temperature, and terminated by the addition of PFA (4% wt/vol), resulting in a cross-linked reaction product. For SR imaging, the reaction product was added to a flow chamber with a presilanized coverslip surface and then incubated for 15 min, resulting in adsorption of the product onto the coverslip. This was followed by a wash of the flow chamber with NEB4 buffer and then the addition of blocking solution (from the previously described SR assay). The surface adsorbed proteins were then labeled and imaged in a manner similar to that described for our SR assay used for imaging cells.

smFRET Assay DNA Preparations. All oligonucleotides were purchased from Integrated DNA Technology. The oligonucleotide sequences are shown in Table S1. For annealing, the appropriate oligonucleotides were mixed and heated for 10 min at 95 °C, followed by slow cooling.

smFRET Reactions. Reactions were carried out at room temperature in a standard buffer composed of NEB4 (20 mM Tris acetate pH 7.5, 10 mM magnesium acetate, 50 mM potassium acetate, and 2 mM DTT), and an oxygen-scavenging system (1 mg/mL glucose oxidase, 0.8% wt/vol glucose, 0.02 mg/mL catalase, and 5 mM Trolox). smFRET assays were performed as described previously (68). In all experiments, 250 pM DNA was immobilized on a PEG-coated glass surface via a biotin-neutravidin linkage. Analysis was performed as described previously (35, 68). Trajectories were weighted equally for histograms, which included a sufficient number of molecules.

ACKNOWLEDGMENTS. We thank N. J. Cowan, J. A. Boroweic, and T. T. Huang for comments on the manuscript, and T. T. Huang and S. B. Crist for assistance with the siRNA and Western blot analyses. Work in E.R.'s laboratory is supported by National Institutes of Health Grants GM057691, GM110385, and GM108119; the Arnold and Mabel Beckman Foundation; a Shifrin–Meyer Breast Cancer Discovery award; and the Ralph S. French Charitable Foundation Trust. D. A. Reid is supported by National Institutes of Health Grant T32 GM088118. Work in D. A. Ramsden's laboratory was supported by National Institute of Health Grant CA08442. Work in M.R.L.'s laboratory was supported by National Institute of Health Grants CA100504 and GM56984.

1. Lieber MR (2010) The mechanism of double-strand DNA break repair by the non-homologous DNA end-joining pathway. *Annu Rev Biochem* 79:181–211.
2. Ramsden DA, Weed BD, Reddy YV (2010) V(D)J recombination: Born to be wild. *Semin Cancer Biol* 20(4):254–260.
3. Weinfeld M, Lees-Miller SP (2012) DNA double-strand break repair by non-homologous end joining and its clinical relevance. *DNA Repair in Cancer Therapy: Molecular Targets and Clinical Applications*, ed Kelley MR, pp 161–189.
4. Lees-Miller SP, Meek K (2003) Repair of DNA double-strand breaks by non-homologous end-joining. *Biochimie* 85(11):1161–1173.
5. Limp-Foster M, Kelley MR (2000) DNA repair and gene therapy: Implications for translational uses. *Environ Mol Mutagen* 35(2):71–81.
6. Friedberg EC (2003) DNA damage and repair. *Nature* 421(6921):436–440.
7. Bonner WM, et al. (2008) GammaH2AX and cancer. *Nat Rev Cancer* 8(12):957–967.
8. O'Driscoll M, Gennery AR, Seidel J, Concannon P, Jeggo PA (2004) An overview of three new disorders associated with genetic instability: LIG4 syndrome, RS-SCID and ATR-Seckel syndrome. *DNA Repair (Amst)* 3(8-9):1227–1235.
9. Grawunder U, et al. (1997) Activity of DNA ligase IV stimulated by complex formation with XRCC4 protein in mammalian cells. *Nature* 388(6641):492–495.
10. Grawunder U, Zimmer D, Kulesza P, Lieber MR (1998) Requirement for an interaction of XRCC4 with DNA ligase IV for wild-type V(D)J recombination and DNA double-strand break repair in vivo. *J Biol Chem* 273(38):24708–24714.
11. Nick McElhinny SA, Snowden CM, McCarville J, Ramsden DA (2000) Ku recruits the XRCC4-ligase IV complex to DNA ends. *Mol Cell Biol* 20(9):2996–3003.
12. Mari PO, et al. (2006) Dynamic assembly of end-joining complexes requires interaction between Ku70/80 and XRCC4. *Proc Natl Acad Sci USA* 103(49):18597–18602.
13. Ahnesorg P, Smith P, Jackson SP (2006) XLF interacts with the XRCC4-DNA ligase IV complex to promote DNA nonhomologous end-joining. *Cell* 124(2):301–313.
14. Buck D, et al. (2006) Cernunnos, a novel nonhomologous end-joining factor, is mutated in human immunodeficiency with microcephaly. *Cell* 124(2):287–299.
15. DeFazio LG, Stansel RM, Griffith JD, Chu G (2002) Synapsis of DNA ends by DNA-dependent protein kinase. *EMBO J* 21(12):3192–3200.
16. Weterings E, Verkaik NS, Brüggenwirth HT, Hoeijmakers JH, van Gent DC (2003) The role of DNA-dependent protein kinase in synapsis of DNA ends. *Nucleic Acids Res* 31(24):7238–7246.
17. Reddy YV, Ding Q, Lees-Miller SP, Meek K, Ramsden DA (2004) Non-homologous end-joining requires that the DNA-PK complex undergo an autophosphorylation-dependent rearrangement at DNA ends. *J Biol Chem* 279(38):39408–39413.
18. Kim JS, et al. (2005) Independent and sequential recruitment of NHEJ and HR factors to DNA damage sites in mammalian cells. *J Cell Biol* 170(3):341–347.
19. Yano K, Chen DJ (2008) Live cell imaging of XLF and XRCC4 reveals a novel view of protein assembly in the non-homologous end-joining pathway. *Cell Cycle* 7(10):1321–1325.
20. Yano K, et al. (2008) Ku recruits XLF to DNA double-strand breaks. *EMBO Rep* 9(1):91–96.
21. Yu Y, et al. (2008) DNA-PK and ATM phosphorylation sites in XLF/Cernunnos are not required for repair of DNA double-strand breaks. *DNA Repair (Amst)* 7(10):1680–1692.
22. Anderson JA, Harper JV, Cucinotta FA, O'Neill P (2010) Participation of DNA-PKcs in DSB repair after exposure to high- and low-LET radiation. *Radiat Res* 174(2):195–205.
23. Reynolds P, et al. (2012) The dynamics of Ku70/80 and DNA-PKcs at DSBs induced by ionizing radiation is dependent on the complexity of damage. *Nucleic Acids Res* 40(21):10821–10831.
24. Yajima H, et al. (2013) The complexity of DNA double-strand breaks is a critical factor enhancing end-resection. *DNA Repair (Amst)* 12(11):936–946.
25. Davis AJ, Chen BP, Chen DJ (2014) DNA-PK: A dynamic enzyme in a versatile DSB repair pathway. *DNA Repair (Amst)* 17:21–29.
26. Hammel M, Yu Y, Fang S, Lees-Miller SP, Tainer JA (2010) XLF regulates filament architecture of the XRCC4·ligase IV complex. *Structure* 18(11):1431–1442.
27. Hammel M, et al. (2011) XRCC4 protein interactions with XRCC4-like factor (XLF) create an extended grooved scaffold for DNA ligation and double-strand break repair. *J Biol Chem* 286(37):32638–32650.
28. Mahaney BL, Hammel M, Meek K, Tainer JA, Lees-Miller SP (2013) XRCC4 and XLF form long helical protein filaments suitable for DNA end protection and alignment to facilitate DNA double-strand break repair. *Biochem Cell Biol* 91(1):31–41.
29. Lu H, Pannicke U, Schwarz K, Lieber MR (2007) Length-dependent binding of human XLF to DNA and stimulation of XRCC4.DNA ligase IV activity. *J Biol Chem* 282(15):11155–11162.
30. Lukas C, Bartek J, Lukas J (2005) Imaging of protein movement induced by chromosomal breakage: Tiny "local" lesions pose great "global" challenges. *Chromosoma* 114(3):146–154.
31. Polo SE, Jackson SP (2011) Dynamics of DNA damage response proteins at DNA breaks: A focus on protein modifications. *Genes Dev* 25(5):409–433.
32. van de Linde S, et al. (2011) Direct stochastic optical reconstruction microscopy with standard fluorescent probes. *Nat Protoc* 6(7):991–1009.
33. Agullo-Pascual E, et al. (2013) Super-resolution fluorescence microscopy of the cardiac connexome reveals plakophilin-2 inside the connexin43 plaque. *Cardiovasc Res* 100(2):231–240.
34. Pavlides SC, et al. (2013) Inhibitors of SCF-Skp2/Cks1 E3 ligase block estrogen-induced growth stimulation and degradation of nuclear p27kip1: Therapeutic potential for endometrial cancer. *Endocrinology* 154(11):4030–4045.
35. Rothenberg E, Grimme JM, Spies M, Ha T (2008) Human Rad52-mediated homology search and annealing occurs by continuous interactions between overlapping nucleoprotein complexes. *Proc Natl Acad Sci USA* 105(51):20274–20279.
36. Rust MJ, Bates M, Zhuang X (2006) Sub-diffraction-limit imaging by stochastic optical reconstruction microscopy (STORM). *Nat Methods* 3(10):793–795.
37. Britton S, Coates J, Jackson SP (2013) A new method for high-resolution imaging of Ku foci to decipher mechanisms of DNA double-strand break repair. *J Cell Biol* 202(3):579–595.
38. Andres SN, Modesti M, Tsai CJ, Chu G, Junop MS (2007) Crystal structure of human XLF: A twist in nonhomologous DNA end-joining. *Mol Cell* 28(6):1093–1101.
39. Tsai CJ, Chu G (2013) Cooperative assembly of a protein-DNA filament for non-homologous end-joining. *J Biol Chem* 288(25):18110–18120.
40. Ochi T, et al. (2012) Structural insights into the role of domain flexibility in human DNA ligase IV. *Structure* 20(7):1212–1222.
41. Ropars V, et al. (2011) Structural characterization of filaments formed by human Xrcc4-Cernunnos/XLF complex involved in nonhomologous DNA end-joining. *Proc Natl Acad Sci USA* 108(31):12663–12668.
42. Andres SN, et al. (2012) A human XRCC4-XLF complex bridges DNA. *Nucleic Acids Res* 40(4):1868–1878.
43. Srivastava M, et al. (2012) An inhibitor of nonhomologous end-joining abrogates double-strand break repair and impedes cancer progression. *Cell* 151(7):1474–1487.
44. Riballo E, et al. (2004) A pathway of double-strand break rejoining dependent upon ATM, Artemis, and proteins locating to gamma-H2AX foci. *Mol Cell* 16(5):715–724.
45. Mao Z, Bozzella M, Seluanov A, Gorbunova V (2008) DNA repair by nonhomologous end-joining and homologous recombination during cell cycle in human cells. *Cell Cycle* 7(18):2902–2906.
46. Walker JR, Corpina RA, Goldberg J (2001) Structure of the Ku heterodimer bound to DNA and its implications for double-strand break repair. *Nature* 412(6847):607–614.
47. Merkle D, Block WD, Yu Y, Lees-Miller SP, Cramb DT (2006) Analysis of DNA-dependent protein kinase-mediated DNA end joining by two-photon fluorescence cross-correlation spectroscopy. *Biochemistry* 45(13):4164–4172.
48. Li Y, Reynolds P, O'Neill P, Cucinotta FA (2014) Modeling damage complexity-dependent non-homologous end-joining repair pathway. *PLoS ONE* 9(2):e85816.
49. Mani RS, et al. (2010) Dual modes of interaction between XRCC4 and polynucleotide kinase/phosphatase: Implications for nonhomologous end joining. *J Biol Chem* 285(48):37619–37629.
50. Abdisalaam S, Davis AJ, Chen DJ, Alexandrakis G (2014) Scanning fluorescence correlation spectroscopy techniques to quantify the kinetics of DNA double-strand break repair proteins after γ-irradiation and bleomycin treatment. *Nucleic Acids Res* 42(1):e5.
51. Pascal JM, O'Brien PJ, Tomkinson AE, Ellenberger T (2004) Human DNA ligase I completely encircles and partially unwinds nicked DNA. *Nature* 432(7016):473–478.

52. Nandakumar J, Nair PA, Shuman S (2007) Last stop on the road to repair: Structure of *E. coli* DNA ligase bound to nicked DNA-adenylate. *Mol Cell* 26(2):257–271.
53. Cary RB, et al. (1997) DNA looping by Ku and the DNA-dependent protein kinase. *Proc Natl Acad Sci USA* 94(9):4267–4272.
54. Leonenko ZV, Merkle D, Shamrakov LG, Lees-Miller SP, Cramb DT (2004) Examination of surface-bound Ku-DNA complexes in an aqueous environment using MAC mode atomic force microscopy. *Biosens Bioelectron* 20(5):918–924.
55. Postow L, et al. (2008) Ku80 removal from DNA through double-strand break-induced ubiquitylation. *J Cell Biol* 182(3):467–479.
56. Lan L, et al. (2010) The ACF1 complex is required for DNA double-strand break repair in human cells. *Mol Cell* 40(6):976–987.
57. Ogiwara H, et al. (2011) Histone acetylation by CBP and p300 at double-strand break sites facilitates SWI/SNF chromatin remodeling and the recruitment of non-homologous end joining factors. *Oncogene* 30(18):2135–2146.
58. Schreiber G, Haran G, Zhou HX (2009) Fundamental aspects of protein–protein association kinetics. *Chem Rev* 109(3):839–860.
59. Yano K, Morotomi-Yano K, Lee KJ, Chen DJ (2011) Functional significance of the interaction with Ku in DNA double-strand break recognition of XLF. *FEBS Lett* 585(6):841–846.
60. Barranco SC, Humphrey RM (1971) The effects of bleomycin on survival and cell progression in Chinese hamster cells in vitro. *Cancer Res* 31(9):1218–1223.
61. Békés M, et al. (2013) DUB-resistant ubiquitin to survey ubiquitination switches in mammalian cells. *Cell Reports* 5(3):826–838.
62. van de Linde S, et al. (2009) Multicolor photoswitching microscopy for subdiffraction-resolution fluorescence imaging. *Photochem Photobiol Sci* 8(4):465–469.
63. Malkusch S, Muranyi W, Müller B, Kräusslich HG, Heilemann M (2013) Single-molecule coordinate-based analysis of the morphology of HIV-1 assembly sites with near-molecular spatial resolution. *Histochem Cell Biol* 139(1):173–179.
64. Henriques R, et al. (2010) QuickPALM: 3D real-time photoactivation nanoscopy image processing in ImageJ. *Nat Methods* 7(5):339–340.
65. Ma Y, Pannicke U, Schwarz K, Lieber MR (2002) Hairpin opening and overhang processing by an Artemis/DNA-dependent protein kinase complex in nonhomologous end joining and V(D)J recombination. *Cell* 108(6):781–794.
66. Roberts SA, et al. (2010) Ku is a 5′-dRP/AP lyase that excises nucleotide damage near broken ends. *Nature* 464(7292):1214–1217.
67. Chan DW, Mody CH, Ting NS, Lees-Miller SP (1996) Purification and characterization of the double-stranded DNA-activated protein kinase, DNA-PK, from human placenta. *Biochem Cell Biol* 74(1):67–73.
68. Rothenberg E, Ha T (2010) Single-molecule FRET analysis of helicase functions. *Methods Mol Biol* 587:29–43.